Article

Effective Visible-Light-Driven Photocatalytic Degradation of Harmful Antibiotics Using Reduced Graphene Oxide-Zinc Sulfide-Copper Sulfide Nanocomposites as a Catalyst

Shanmugam Mahalingam, Yalini Devi Neelan, Senthil Bakthavatchalam, Latifah A. Al-Humaid, Nora Dahmash Al- Dahmash, Harikrishnan Santhanam, Tae-Youl Yang, Nazmul Hossain, Sung Heum Park, and Junghwan Kim*

Read Online

ACCESS | Metrics & More | Article Recommendations | SI Supporting Information

ABSTRACT: In recent decades, antibiotics have been found in aquatic environments, raising severe concerns. In this study, a unique reduced graphene oxide-zinc sulfide-copper sulfide (rGO-ZnS-CuS) nanocomposite (NC) prepared by using a straightforward surfactant-free *in situ* microwave method was used for antibiotic degradation via photocatalysis. The structural and morphological characteristics of the produced catalysts were characterized using various techniques, confirming the successful development of nanocomposite structures of better quality than that of the pure samples. The photocatalytic degradation of antibiotics containing ofloxacin was also investigated. The results suggest that the rGO-ZCS NC outperformed the other composites in terms of photocatalytic activity toward ofloxacin degradation. Superoxide and hydroxyl radicals were the main active species during the degradation process. According to our results, the catalytic activity of rGO-ZCS NC is much better than that of the other composites.
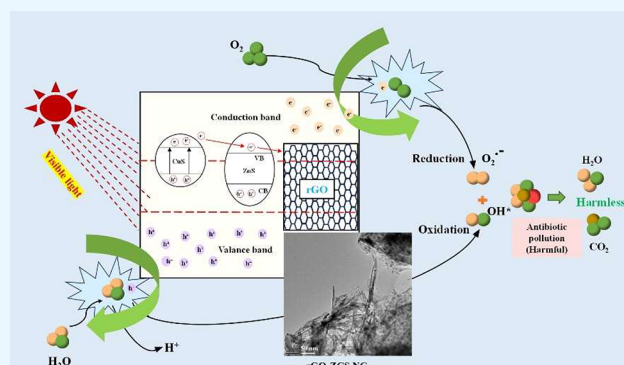
1. INTRODUCTION

In recent decades, environmental problems have become a global concern due to the rapid establishment of industries and societies.[1,2] Due to the accumulation of domestic sewage and wastewater discharges containing organic pollutants, including phenols, pesticides, and antibiotics, the proliferation of the dyeing and printing industries severely damages both humankind and the environment by causing health issues and affecting the ecosystem.[3−5] Over 3000 chemical substances, including pharmaceutical compounds, whose concentration ranges from ng/L to μg/L, are generally found in wastewater, surface water, soil, groundwater, and drinking water worldwide.[6−8] In particular, pharmaceutical antibiotics and their derivatives, which result from the medical treatment of humans and from the farming industry, are considered emerging pollutants that raise public concerns.[7,9] Among the many pharmaceutical compounds, antibiotics are found in various aqueous environments.[10,11] In 2010, the amount of antibiotics consumed in stock farming was approximately 63,200 tons worldwide and is expected to increase by two-thirds, to approximately 105,600 tons, by the year 2030.[12] The antibiotics that reach aquatic ecosystems are derived from various sources, including hospital effluents, livestock and human excretion, and the pharmaceutical industry.[13] Anti-

biotics are chemotherapeutic agents used to treat bacterial infections. They were developed to limit the mortality rate and boost the immune system of animals and humans.[14] However, only 30% of the developed antibiotics are being used to fight diseases in animals and humans, and the other 70% are badly deflected toward the environment without being metabolized.[10,15] Most of the antibiotics in the environment are poorly metabolized and can be consumed by both animals and humans; therefore, their consumption may pose a serious threat to the ecosystem, as well as the spread and development of antibiotic resistance genes and antibiotic-resistant bacteria.[9] An easy method to reduce the propagation of bacterial resistance and the environmental toxicity of antibiotics is by adequately treating wastewater that contains antibiotics before discharging it into the environment.[16]

Numerous techniques have been studied extensively and adopted to remove antibiotics from different media, including
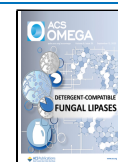
membrane filtration, adsorption, wastewater chemical and physical treatment, advanced oxidation processes, piezoelectric catalysis, reverse osmosis, electrocoagulation, biological treatment, ion exchange, and microbial degradation technology.[17] Among the various techniques used, photocatalytic degradation is regarded as a promising and sustainable method to convert pollutants into harmless products owing to the following advantages: no secondary pollution, easy operation, low cost, nontoxicity, being a green method, and high pollutant degradation efficiency.[3,1] Organic pollutants are widely degraded using a photocatalyst.[17] Photocatalytic degradation is an emerging technology that uses light as an energy source to activate chemical reactions and nanoscale catalysts.[17] High mineralization percentages can be obtained using a photocatalytic process.[3,18,19] Among pharmaceutical compounds, antibiotics are some of the main contributors to severe environmental contamination because of their high consumption rates in both human and veterinary medicine. Pharmaceutical compound degradation using semiconductor photocatalysts is a viable option because of advantages such as low cost, energy savings, environmental friendliness, simplicity, and mild reaction conditions. Therefore, establishing and fabricating a stable, inexpensive, visible-light-driven, effective, and efficient catalyst for the decomposition of organic pollutants is of great significance.[6]

Because of its simplicity, the lack of secondary contamination, and the fact that it uses direct sunlight, photocatalytic degradation has been hailed as a sustainable and promising approach for transforming pollutants into innocuous compounds. Most photodegradation studies are based on ultraviolet (UV) light; however, continuous exposure to UV light leads to serious health issues, such as skin cancer, premature aging, and blinding eye diseases. Moreover, the availability of UV light in solar radiation is only 4−5%, whereas that of visible light is approximately 40%. Owing to the wide availability of visible light and its zero harmful effect on human health, the use of visible light in photodegradation has attracted the attention of researchers. Various traditional materials, including CuO/ZnS, CdS/ZnO, ZnO/ZnS, and CdS/ZnS, have been reported to be useful for this purpose. Zinc sulfide has gained attention from researchers because of its wide bandgap, nontoxicity, good stability, low cost, abundance, and strong fluorescence.[20] Doping ZnS with foreign elements successfully enhances its absorbance in the visible light region.[21] Metal oxide nanoparticles with reduced graphene oxide are expected to increase the charge transfer between the metal oxide and organic dye molecules, ultimately resulting in enhanced photodegradation properties. The main advantages of using carbon-based materials in photodegradation studies are their excellent electrochemical properties and large specific surface area.[9] In recent decades, CuS semiconductors have been shown to be excellent candidates for visible-light photocatalysis because of their good optical absorption properties and narrow bandgap.[22] Hazardous pollutants in aqueous environments can be decomposed using heterostructures in semiconducting nanocomposites because of their excellent properties that improve the charge transfer mechanism and slow the fast recombination of charge carriers.[6] Thus, an enhanced activity of the active radicals can be achieved during antibiotic photodegradation owing to the excellent chemical and physical properties of the heterostructure.[23]

Here, visible-light-driven reduced graphene oxide-zinc sulfide-copper sulfide nanocomposites (rGO-ZCS NCs) were prepared using a one-step rapid and environmentally friendly microwave-assisted synthesis method. By loading different amounts of CuS-ZnS onto rGO, its morphology, chemical composition, and photocatalytic performance were characterized using SEM. Moreover, it was used for the oxidative photodegradation of ofloxacin (OFL), an organic pollutant, under visible light irradiation. To the best of our knowledge, OFL degradation using the rGO-ZCS NC has not been completely explored, and limited information is available regarding its use for the treatment of compounds in aqueous media. Therefore, the results of the present study will be useful for the future visible-light-driven photocatalytic degradation of antibiotic compounds.

2. MATERIALS AND METHODS

2.1. *In Situ* Microwave Synthesis of rGO-ZCS NCs.
The *in situ* microwave technique was used to prepare the GO-ZCS NCs. An initial suspension of 100 mg of GO in 100 mL of deionized (DI) water was ultrasonically sonicated for 90 min. Subsequently, 0.1 mM each of $ZnSO_4 \cdot 7H_2O$ and $CuSO_4 \cdot 5H_2O$ was added to the GO suspension with continuous stirring for 2 h. The suspension was then microwaved at 950 W for 10 min using a microwave oven. The suspension was left to cool to room temperature. Thereafter, for the *in situ* reduction of GO to rGO, 100 mg of thiourea was added to the suspension, and the mixture was continuously stirred for 2 h. The solution was then microwaved as described previously. The rGO-ZCS NC solution was centrifuged multiple times and washed using DI water and ethanol. The cleaned solid products were then dried overnight at 80 °C using a hot air oven to obtain the rGO-ZCS NCs.[24]

2.2. Characterization.
X-ray diffraction (XRD, D8 advance, Bruker, Germany) was performed using $CuK\alpha$ radiation ($\lambda = 1.5406$ Å) at 40 kV and 30 mA. Field emission scanning electron microscopy (FE-SEM, S-4200, Hitachi, Japan) was conducted, and energy-dispersive X-ray spectroscopy (EDX) was performed to produce elemental maps. The morphology of the synthesized hybrid nanocomposites was analyzed using high-resolution transmission electron microscopy (HR-TEM, FEI-Tecnai TF-20), and the selected-area diffraction (SAED) patterns were obtained at an accelerating voltage of 200 kV. The functional groups in the product were studied using Fourier transform infrared spectroscopy (FTIR) in the 4000−500 cm^{-1} range using a Nicolet-iS10 spectrometer (USA). The surface area and pore size were analyzed by using a Quantachrome/Autosorb-iQ analyzer, and the OFL concentration was determined by measuring the absorbance of the solution at 288 nm using a UV−vis spectrophotometer.

2.3. Photodegradation Experimental Procedure.
The photocatalytic activity of the prepared nanocomposites was evaluated at ambient temperature by examining the photocatalytic decomposition of an OFL solution under visible-light irradiation ($\lambda = 400$ nm) using a tungsten lamp (300 mW/cm^{-2}). Generally, in the experimental procedure, a known dosage of the photocatalyst (20 mg) was mixed with a fixed volume of a solution (i.e., 100 mL) of OFL (0.04 mmol). The mixture was magnetically stirred for 30 min in the dark before exposure to light irradiation at room temperature to attain the adsorption−desorption equilibrium between the catalyst and the organic pollutant. Subsequently, the mixture was irradiated with visible light to initiate the photocatalytic reaction. A volume of 3 mL of the solution was collected every 15 min and

was centrifuged, and its absorbance was occasionally measured using a UV−vis spectrophotometer.

3. RESULTS AND DISCUSSION

3.1. Structural Analysis. XRD measurements were performed to analyze the phase formation and crystalline structures of the prepared samples. Figure 1a shows the
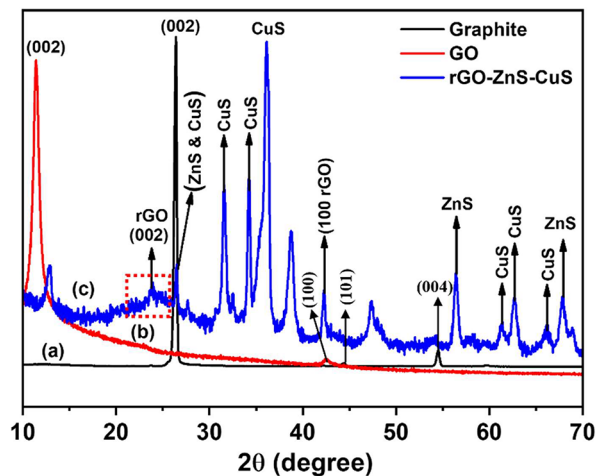

Figure 1. XRD analysis of (a) graphite, (b) GO, and (c) rGO-ZnS-CuS NCs using a microwave-assisted synthesis method.

graphite XRD pattern, with a prominent peak at 26.4° corresponding to the (002) plane of the hexagonal structure. Two more peaks at 44.4° and 54.5°, which correspond to the (101) and (004) planes, respectively, can be observed. Figure 1b shows the XRD pattern of GO. The peaks at 11° and 42°

are attributed to the GO planes (002) and (100), respectively. Thus, formation of the sp^2-bonded carbon atom was confirmed. Figure 1c shows the XRD patterns of the prepared nanocomposites. Because of the technique used for the preparation of the materials, GO was converted to rGO, which can be observed from the XRD results by the broadening and low-intensity peak at 23.82°. The XRD graph of the rGO-ZCS NCs shows that the CuS (JCPDS No: 06−0464) nanoparticles exhibit several diffraction peaks at 26.43°, 31.47°, 34.28°, 36.05°, 61.36°, 62.71°, and 66.17°, which belong to the planes (101), (102), (103), (006), (110), (108), and (116), respectively. Moreover, the peaks at 26.43°, 56.47°, and 67.86° correspond to the planes (111), (220), and (311) of the ZnO nanorods (JCPDS No: 65−1691).[24] Thus, these peaks confirm the presence of ZnO nanorods and CuS nanoparticles on the rGO sheets with no other trace impurity peaks. Hence, the XRD patterns revealed the successful formation of the rGO-ZCS NC.

3.2. Morphological Studies of rGO-ZCS NC via FE-SEM and EDX Analyses. The microstructure and morphology of the prepared rGO-ZCS NCs were analyzed by using FE-SEM at different magnifications. Figure 2 shows the densely packed ZnS nanorods and CuS nanoparticles decorating the rGO nanosheets. The typical crumpled structure of the rGO nanosheets is clearly seen in Figure 2a and b, whereas the nanoparticles and nanorods decorating the rGO sheets can be observed in Figure 2c and d. The surface chemical composition of the prepared rGO-ZCS NCs was examined using EDX. Five distinct peaks corresponding to Zn, S, Cu, C, and O, which were present in the prepared samples, were identified via a quantitative elemental analysis using EDX (Figure 2f).[25] The EDX results confirmed the high crystallinity of the sample prepared by using the *in situ* microwave synthesis method.
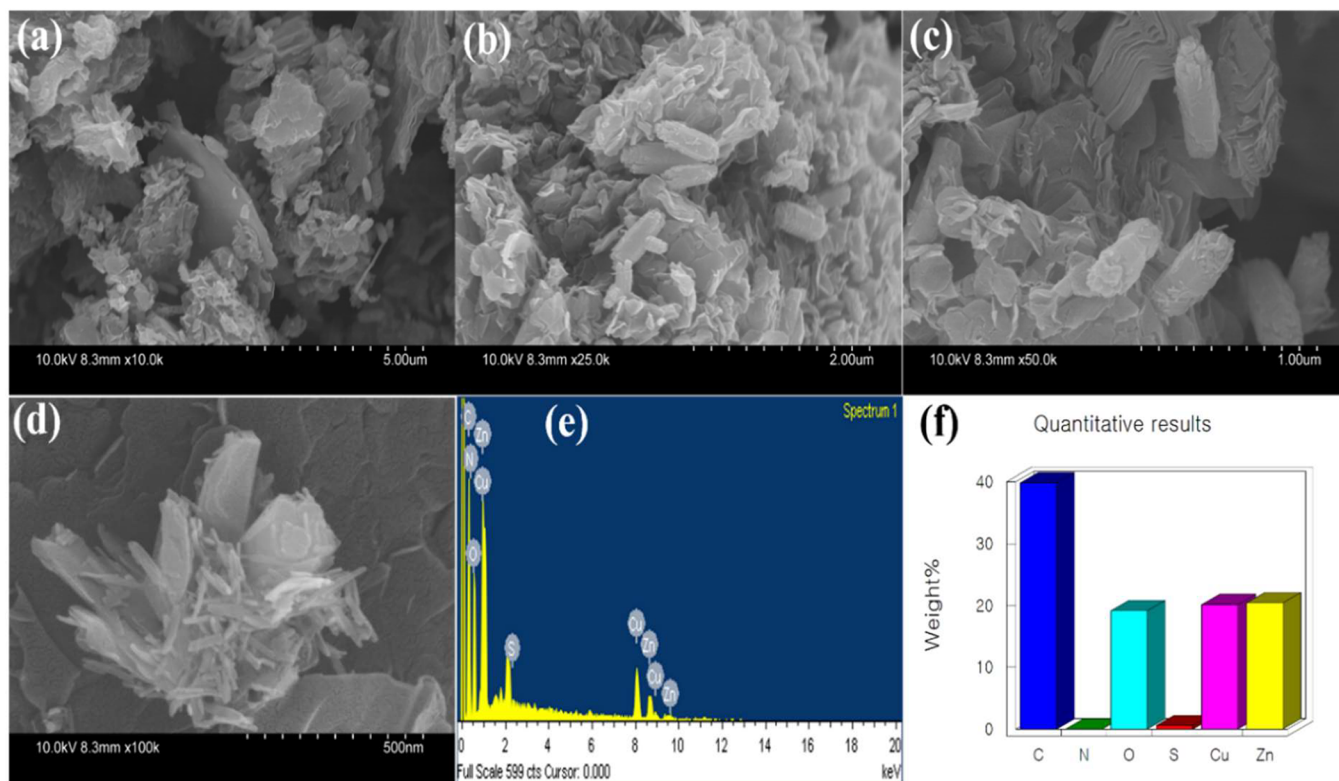

Figure 2. SEM (a−d) and EDX and quantitative analysis (e−f) images of the rGO-ZCS NC samples prepared using an *in situ* microwave method.
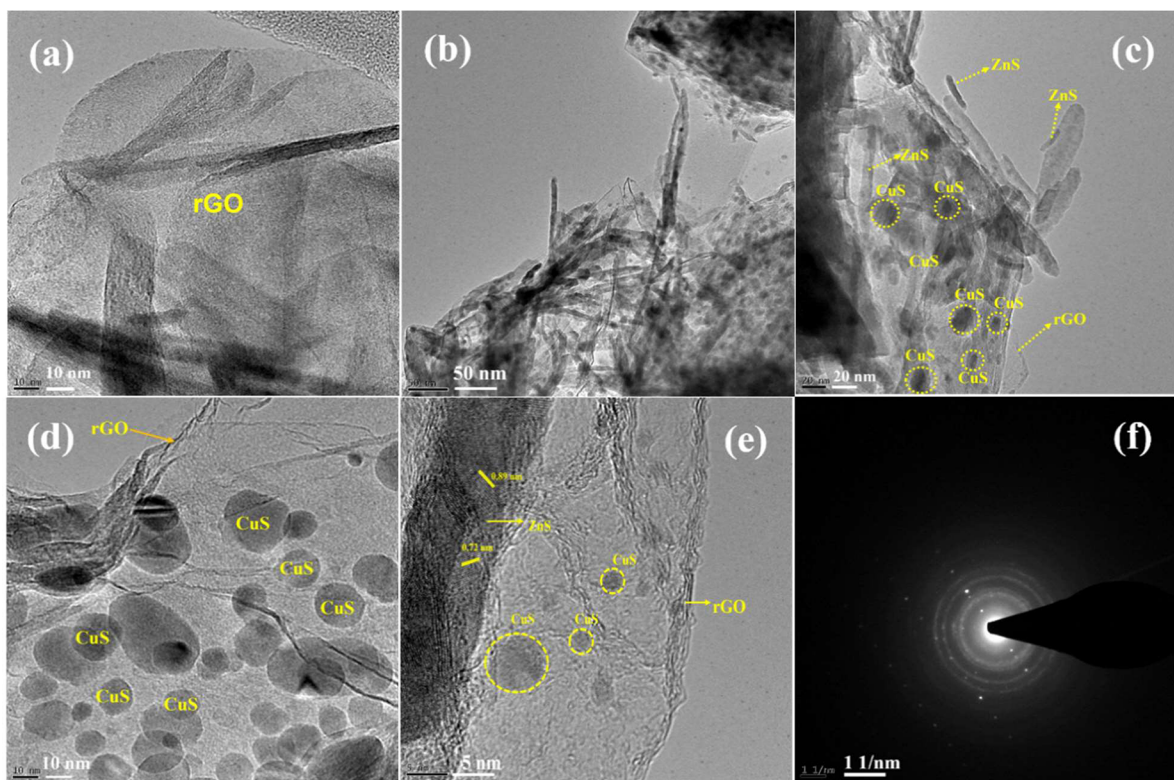
Figure 3. HR-TEM images of (a) pure rGO, (b−e) higher magnified images, and (f) SAED pattern of the rGO-ZCS NC.
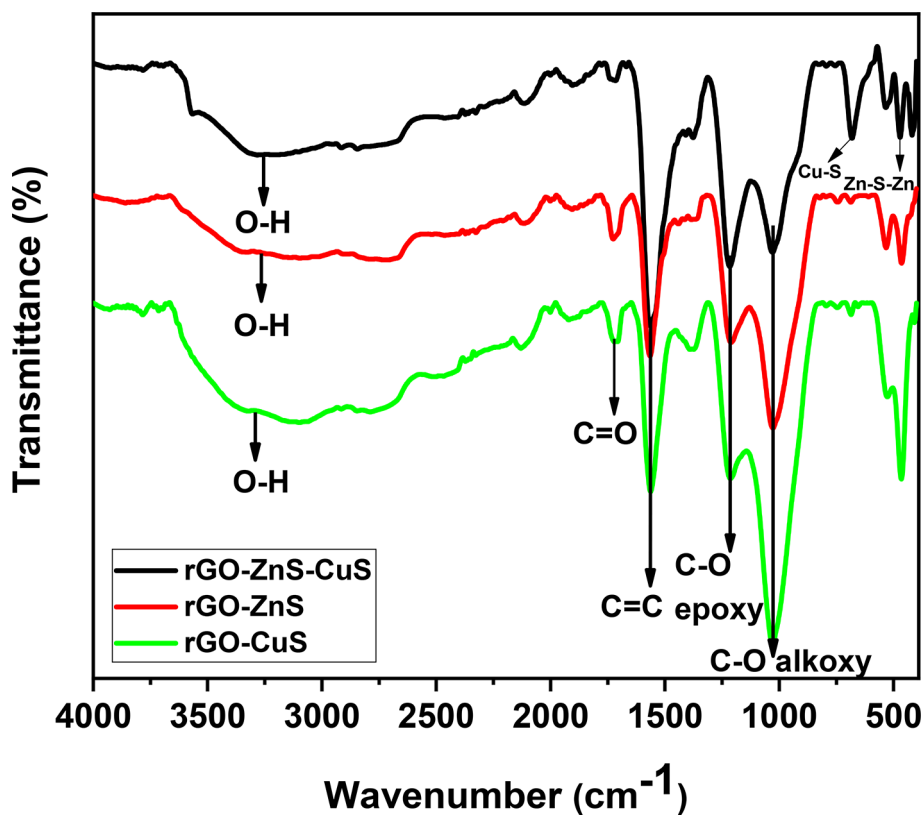

Figure 4. Results of the FTIR analysis of the rGO-ZCS NC.

3.3. HR-TEM and SAED Pattern of the Prepared rGO-ZCS NCs. The surface morphology and lattice fringe pattern of the rGO-ZCS NCs prepared via *in situ* microwave synthesis are shown in Figure 3. Figure 3a shows the folded and thin morphologies of the few-layered rGO nanosheets. The higher-magnification images (Figure 3b−d) clearly show that the ZnS
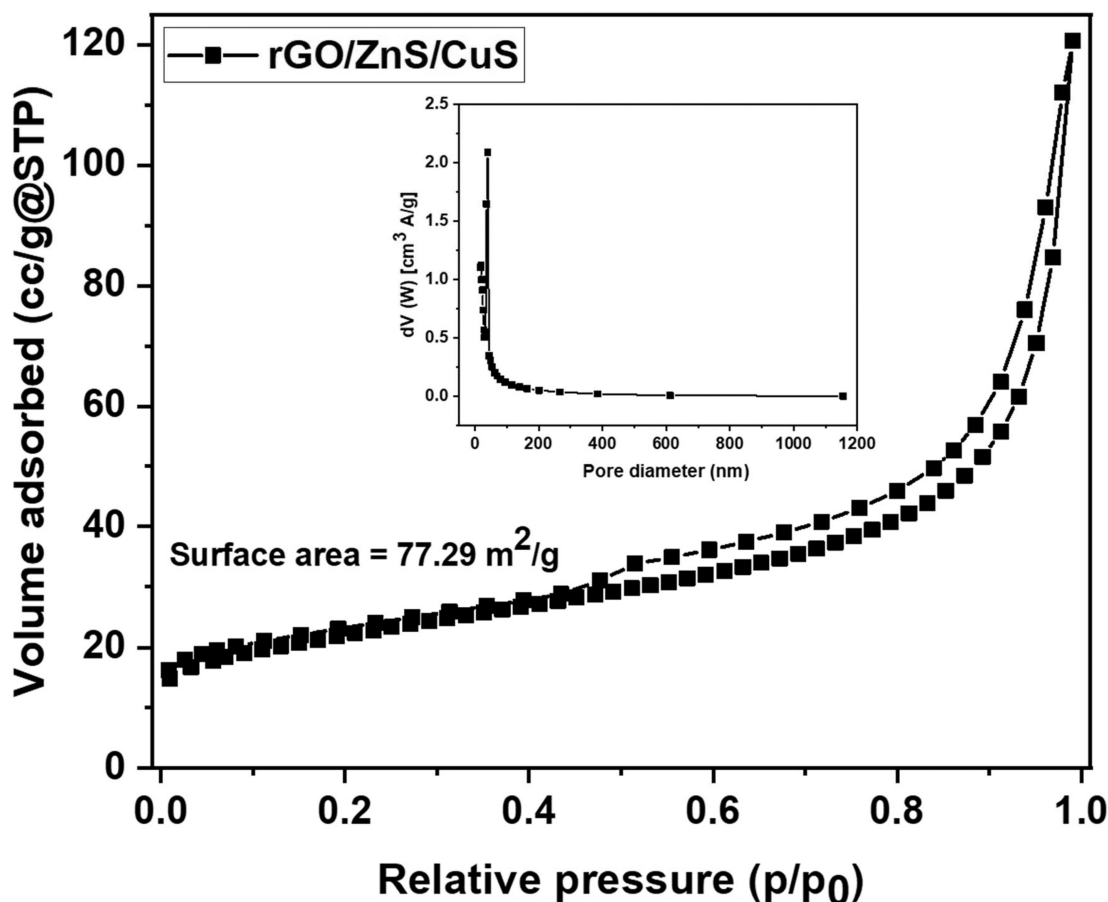
Figure 5. Results of the surface area analysis of the rGO-ZCS NC using BET.

nanorods and CuS nanoparticles decorate the interlayer of the rGO nanosheets. The sizes of the ZnS nanorods and CuS nanoparticles were determined to be approximately 60 and 25 nm (diameter), respectively, based on the HR-TEM images. Furthermore, the fringe patterns of ZnS and CuS, which are visible in Figure 3e, confirm the crystalline structure of the synthesized NC. The bright spots and concentric circles of the prepared rGO-ZCS NC can be clearly observed in the SAED patterns. This study reveals that the prepared material is polycrystalline. ZnS and CuS are associated with bright spots, whereas the circles in the rGO nanosheets indicate the incorporation of the particles into the nanosheets of the prepared nanocomposites.[24] Thus, the successful preparation of nanocomposites using the *in situ* microwave synthesis method was confirmed by the HR-TEM results.

3.4. FTIR Analysis of the rGO-ZCS NC. The differences in the oxygen-containing functional groups of the ZnS- and CuS-decorated rGO NCs were analyzed by using FTIR spectroscopy. The characteristic peaks of rGO and the other functional groups can be clearly observed in Figure 4. The characteristic peak at 3260 cm^{-1} is associated with the bending and stretching vibrations of the O$-$H group. The C$=$O bond involves stretching vibrations of the carbonyl and carboxyl groups, which correspond to the peak at 1726 cm^{-1}. Additionally, the peak at 1218 cm^{-1} corresponds to the stretching vibration of the C$-$O bond of the epoxy group[21] and the peak at 1031 cm^{-1} corresponds to the C$-$O alkoxy stretching vibration. The peak at 1613 cm^{-1} is attributed to the stretching vibration of the C$=$C bond of the sp^2-hybridized

graphitic carbon.[26] ZnS and CuS have distinct absorption bands at 472 cm^{-1} (Zn$-$S$-$Zn vibration) and 685 cm^{-1} (Cu$-$S stretching vibration), respectively. These bands correspond to those reported in the literature.[27,28]

3.5. Surface Area Analysis Using Brunauer$-$Emmett$-$Teller (BET). The nitrogen adsorption$-$desorption isotherm resulting from the BET surface area analysis of the rGO-ZCS NC is shown in Figure 5. The introduction of rGO onto the heterostructure nanocomposite provided more active sites for the photocatalytic degradation reaction. The adsorption efficiency of the prepared nanocomposites before the adsorption$-$desorption equilibrium was reached was calculated and determined to be 77.29 m^2/g. According to the calculations using the BJH method, the NCs had pores with a volume of 0.174 cc/g and a size of 1.317 nm.[29] Thus, the rGO-based nanocomposites clearly showed good adsorption efficiency toward OFL, due to which the diffusion distance in the reactive oxidative species grew on the surface of the catalyst and resulted in an enhanced photocatalytic performance. Thus, the introduction of rGO into the nanocomposites obviously enhanced the photocatalytic performance of the rGO-ZCS NC.[26] The BET surface area analyses of the rGO/CuS and rGO/ZnS are also given in Figure S1.

3.6. Photocatalytic Decomposition of OFL under Visible-Light Irradiation. OFL was used to examine the photocatalytic activity of the prepared rGO-ZCS nanocomposites under visible light irradiation, as depicted in Figure 6. The absorption spectra of the mixture of OFL and rGO-ZCS NCs under visible-light irradiation for various
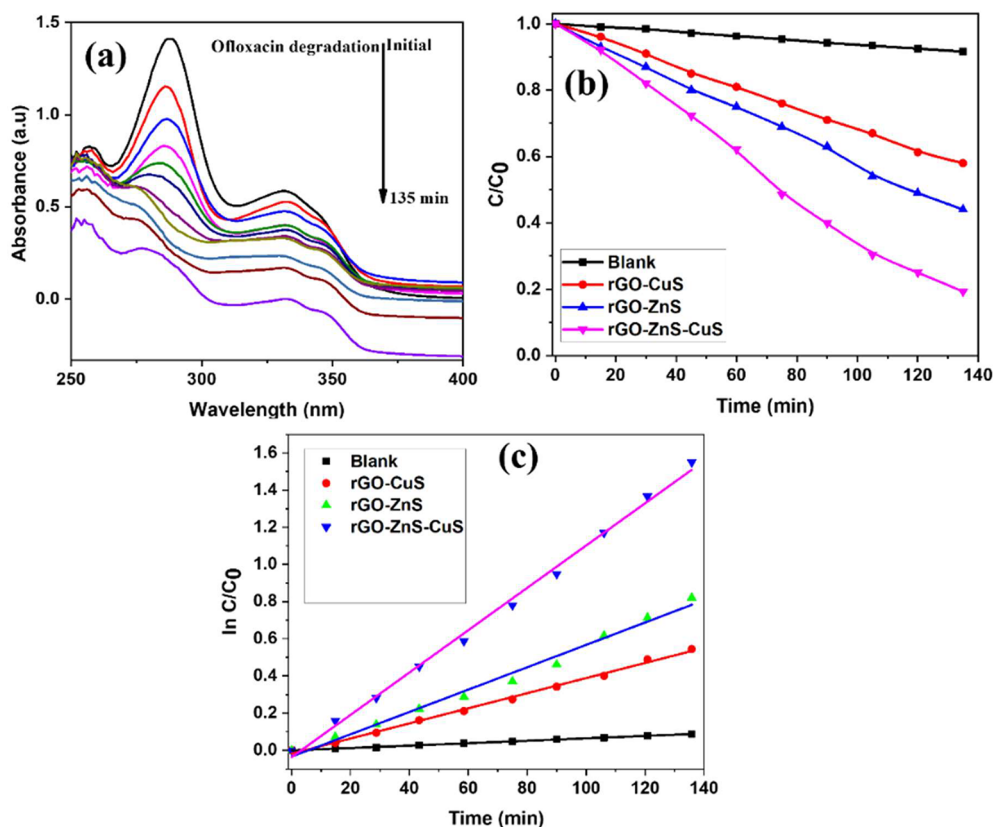
Figure 6. OFL photocatalytic degradation under different conditions: (a) rGO-ZCS NCs and visible-light irradiation; (b) C/C_0 vs time for the different catalysts; (c) pseudo-first-order kinetic $\ln[C_0/C]$ vs time plots for the different catalysts.
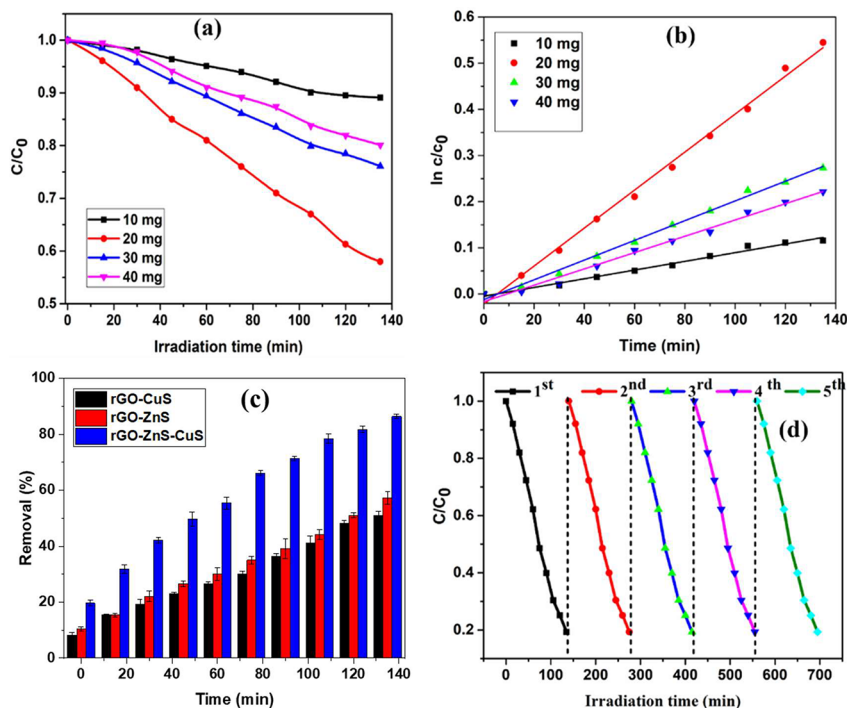

Figure 7. OFL photocatalytic degradation using (a) various dosages of rGO-ZCS NC; (b) pseudo-first-order $\ln[C_0/C]$ vs time kinetic plots for the various dosage levels; (c) OFL removal (%) vs time when using different catalysts; and (d) recycle stability test of the rGO-ZCS NC for five cycles.

durations are shown in Figure 6a. OFL decomposed rapidly after 135 min when the rGO-ZCS NCs were activated by irradiation with visible light (Figure 6a). Generally, the

photocatalytic performance of a catalyst is based on (i) the separation efficiency of the photoexcited electron−hole pairs and (ii) the amount of reactive oxygen species.[21,30] When

exposed to visible-light irradiation, ZnS does not respond because of its large bandgap, whereas CuS is active under these conditions. Therefore, forming a heterostructure network between ZnS and CuS to shift the photogenerated electrons from the conduction band of CuS to that of ZnS is necessary. This leaves a trace of holes in the valence band of CuS, which results in a decrease in the recombination of electron–hole pairs that occurs and thereby an increase in photocatalytic activity, as shown in Figure 6.

The GO-based NC materials showed strong absorption over the entire scanning range; thus, the absorption of the CuS/ZnS-decorated rGO NCs was stronger than that of the rGO-decorated NCs, which might be due to the increased rGO content. When an appropriate amount of introduced graphene, which acts as a macromolecular "photosensitizer", is irradiated with visible light, the electrons on the highest occupied molecular orbital of graphene are excited to its lowest unoccupied molecular orbital. Subsequently, the excited electrons from the graphene shift to the conduction band of ZnS, which results in the separation of the electron–hole pairs. Therefore, for the above-mentioned reasons, the number of photoexcited electrons in the conduction band of ZnS was increased by the addition of graphene. Therefore, the introduction of the appropriate percentage of rGO enhances the optical properties of the NCs, making these excellent photocatalysts for the decomposition of antibiotic pollutants.

Figure 6b shows the photocatalytic efficiencies of the blank and rGO-ZnS, rGO-CuS, and rGO-ZCS NC photocatalysts. In the absence of the photocatalyst, no significant changes were observed in the concentration of ofloxacin during photocatalytic degradation in the dark. Under visible-light irradiation, the OFL concentration remained stable. Under visible-light irradiation, a maximum decomposition of 86.65% was obtained within 135 min using the rGO-ZCS NC. The decomposition efficiency percentages at 135 min for the rGO-ZnS, rGO-CuS, and rGO-ZCS NC were 57.43%, 51.15%, and 86.65%, respectively. The degradation of OFL decreased with time according to the pseudo-first-order kinetic model, as shown in Figure 6c. The first-order kinetic constants corresponding to the decomposition of ofloxacin using various catalysts, such as pure material, rGO-ZnS, rGO-CuS, and rGO-ZCS NC, were determined. The rate constant of the degradation of OFL was 0.01139 min/h, which is consistent with the pseudo-first-order kinetic linearity model.

OFL photocatalytic degradation using various dosages of rGO-ZCS NC, pseudo-first-order kinetic plots, OFL antibiotic removal (%), and cycle stability tests is shown in Figure 7. The photocatalytic performance of the prepared nanocomposites was analyzed based on the photocatalytic decomposition of OFL under visible light irradiation. First, the photocatalytic degradation of the pure rGO-ZnS, rGO-CuS, and rGO-ZCS NC was performed. Further analysis of the photocatalysis was carried out by increasing the rGO-CZS dosage to 10, 20, 30, and 40 mg, and a similar degradation procedure was performed.

To determine the ideal photocatalyst load for the various photocatalyst weights (10, 20, 30, and 40 mg), a series of experiments was carried out (Figure 7a). The removal and decomposition efficiencies of photocatalysts at weight ratios of 10, 20, 30, and 40 mg were 38.7%, 86.6%, 62.3%, and 54.4%, respectively. Notably, with an increasing catalyst loading, the rate of OFL removal steadily increased from 10 to 20 mg, and then decreased. The amount of adsorbed OFL molecules also

increased with an increasing photocatalyst loading. Because the photocatalyst is visible-light-resistant, the reduction of the ofloxacin concentration at the maximum catalyst loading of 40 mg indicates an effective catalytic removal.[31] The photon resistance induced by the catalyst particles and rGO sheets in the composite material leads to a higher amount of photocatalyst present, which reduces the photocatalytic removal efficiency. Since the catalyst was loaded to its full capacity, a shading effect occurred, which reduced the ability of the catalyst to absorb visible light and severely resisted photons, thereby decreasing the efficiency of the catalytic breakdown.[32]

The rates constant of the pseudo-first-order kinetics curves for the ternary catalyst doses of 10, 20, 30, and 40 mg, which are depicted in Figure 7b, are 0.0145, 0.0686, 0.0430, and 0.0233 min, respectively. The optimal amount of catalyst for the most effective degradation of OFL using the rGO-ZCS NC was 20 mg. The photocatalytic performance of the rGO-ZCS NC was better than those of the pure sample and the other samples, eliminating more than 86.65% of the OFL in 135 min (Figure 7c). From these results, 20 mg of rGO-ZCS NC can clearly eliminate more pollutants from the prepared sample for the same irradiation time and leads to a better photocatalytic decomposition rate than those obtained using the other NCs. The photocatalytic performance of the rGO-ZCS NC heterostructure (20 mg) significantly enhanced OFL decomposition.

Ternary photocatalysts must be stable and reusable for practical application. Several cycles of ofloxacin treatment with the rGO-ZCS NC (20 mg) catalyst were performed under visible-light irradiation to evaluate its cycle stability. For each run, the catalyst was recovered via centrifugation, washed with DI water, and dried for 12 h at 60 °C. Based on the cycle test results, the resultant photocatalyst was used for the subsequent catalyst runs (Figure 7d). In the fifth cycle, the photocatalytic decomposition efficiency decreased slightly. The effectiveness of this decrease is related to the dissolution and photocorrosion of the catalyst.

The degradation efficiency of OFL can be calculated using eq 1:

$$D(\%) = \frac{(C_0 - C)}{C_0} \times 100\% \tag{1}$$

where C_0 is the absorption of OFL after the adsorption equilibrium is achieved before visible-light irradiation and C_t is the absorption of OFL in the time interval t under visible light irradiation. The photocatalytic kinetics are expressed as in eq 2:

$$\ln\frac{C_0}{C_t} = Kt \tag{2}$$

where K is the pseudo-first-order reaction rate constant and t is the irradiation time.

The rate constants of OFL degradation in the prepared samples are listed in Table 1.

3.7. Mechanism of the Photodegradation of the rGO-ZCS NC. The photocatalytic degradation of OFL was proposed and demonstrated in this study. Here, a heterostructure of rGO-ZCS NC was developed and used effectively owing to the wide bandgap of ZnS (n-type) and the narrow bandgap of CuS (p-type). CuS was loaded preferentially onto the surface of ZnS to form a close interaction between ZnS and

Table 1

sample	degradation (%)	rate constant (min^{-1})	R^2 value
rGO-ZnS	57.43	0.00601	0.9862
rGO-CuS	51.15	0.00406	0.97629
rGO-ZnS-CuS	86.65	0.01139	0.99624

CuS. The separation of the photoexcited electron−hole pair and the simultaneous enhancement of the photocatalytic degradation are believed to be due to the presence of different bandgaps and interfacial contacts. Under simulated light irradiation, both semiconductor materials can fully utilize the optical energy to separate the photoexcited holes and electrons from the valence and conduction bands, respectively.[33] By introduction of rGO onto the heterostructure of the ZnS/CuS nanocomposites, the photogenerated electrons effectively transferred to the conduction bands of the rGO, thereby improving charge separation and suppressing charge recombination. The separated holes in the valence bands of ZnS and CuS effectively oxidize H_2O into hydroxyl radicals ($OH^{\bullet}$).[34,35] In addition, owing to the existence of O_2 in the prepared solution, the transferred electrons at the rGO can produce superoxide radicals ($O_2^{\bullet-}$), and the superoxides also tend to react with hydrogen peroxide (H_2O_2) dissociating into $OH^{\bullet}$ radicals.

Furthermore, the surface of rGO is enriched with residual functional groups, such as hydroxyl and carboxyl groups. When exposed to light, photons are absorbed by ZnS and CuS, generating excitons. These photoexcited electrons then interact with the residual functional groups on the rGO, leading to an increase in oxide radicals ($O_2^{\bullet-}$) through the reduction in the conduction band. Consequently, the $OH^{\bullet}$ and $O_2^{\bullet-}$ radicals react with antibiotic pollutants and degrade them into nontoxic and inorganic products (e.g., H_2O and CO_2). The operating

mechanism is illustrated in Figure 8. The photocatalytic degradation enhancement is thought to be mainly due to the introduction of rGO onto the heterostructure of ZnS/CuS nanocomposites. The rGO captures the photoinduced electrons from the ZnS/CuS, thus resulting in effective suppression of the recombination of charge carriers and allowing more photoexcited electrons and holes to participate in the photocatalytic decomposition process, which results in an improved OFL degradation performance.

The additional photoelectrochemistry properties of rGO-ZCS NC, rGO-ZnS and rGO-CuS are provided in the Supporting Information.

A comparison of the photocatalytic degradation of antibiotic pollutants using rGO/metal oxide NC-based catalysts is shown in Table 2.

4. CONCLUSIONS

The present study focused on the preparation of rGO-ZCS NC using an in situ microwave technique. The photocatalytic degradation of ofloxacin was analyzed using the synthesized nanocomposites. The structural, morphological, and optical properties of the synthesized catalysts were investigated to confirm the formation of nanocomposite hybrids with enhanced features compared with those of the pure ZCS NC. The incorporation of rGO into the ZCS NC improved the photocatalytic activity due to the synergistic effect of the composites. The rGO acts as an excellent electron conductor, facilitating the efficient transport of photogenerated electrons. Additionally, ZCS serves as a photosensitizer, effectively capturing photons and transferring the generated charge carriers to rGO. This synergistic effect improves theoverall photocatalytic activity by enhancing charge separation and suppressing recombination. Thus, the synthesized composites outperformed the pure ZCS NCs and other composites.
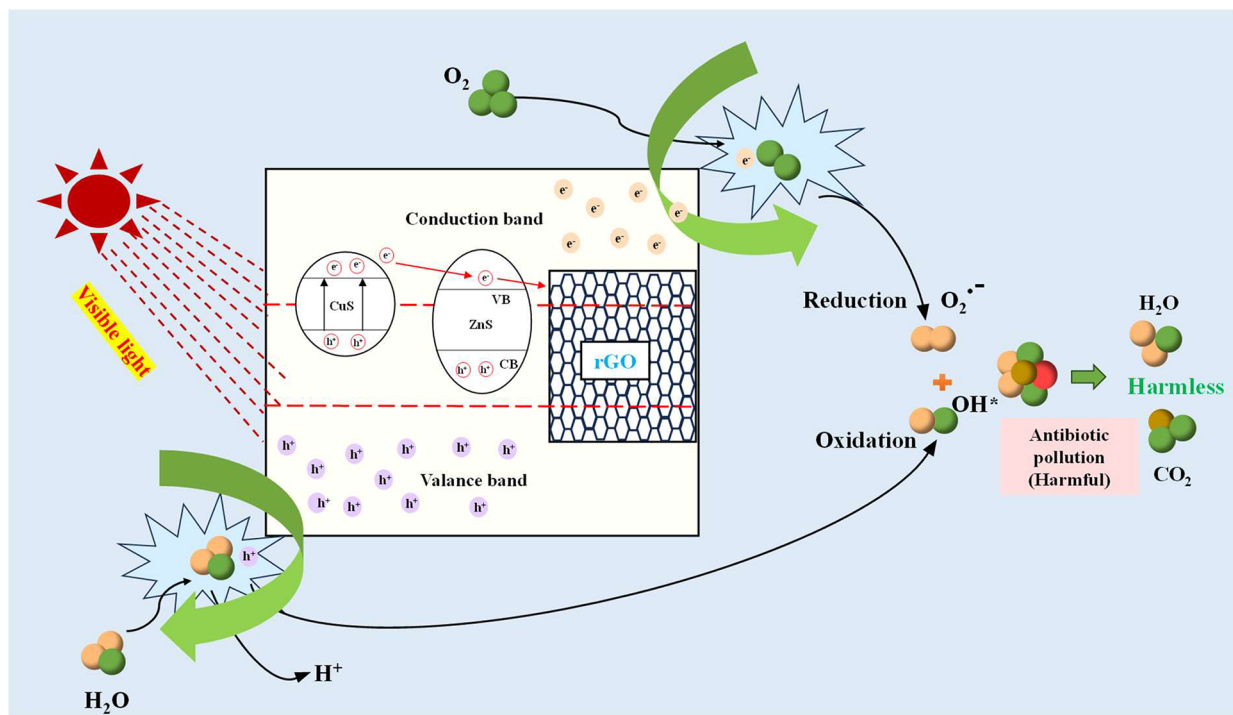

Figure 8. Schematic representation of the mechanism underlying the photodegradation of the prepared rGO-ZCS NC under visible-light irradiation.

Table 2

sample	photocatalyst	antibiotics	cat. wt.	efficiency (%)	light source	ref
1.	rGO-ZnO nanocomposite	CAP antibiotics	0.1−1.0 g	91	UV light	36
2.	$Ce_2Zr_2O_7$@rGO	Ciprofloxacin	100 mg	89	UV light 250 W Hg lamp	37
3.	NiFe-LDH/rGO	Moxifloxacin	100 mg	63	10 W LED lamp	38
4.	$ZnSnO_3$/rGO	Metronidazole	100 mg	73	UV light 500 W Xe lamp	39
5.	$BiVO_4$/rGO aerogel	Formaldehyde (HCHO)	50 mg	60	UV light 150 W Xe lamp	40
6.	C_3N_4@$MnFe_2O_4$-G	Metronidazole	100 mg	78	UV light 300 W Xe lamp	41
7.	Fe_3O_4@TiO_2-GO	Enrofloxacin	400 mg	96/(240 min)	UV light 500 W Xe lamp	42
8.	NiAl LDH/Fe_3O_4-rGO	Ciprofloxacin	250 mg	91/(150 min)	UV light 500 W Xe lamp	43
9.	PANI-TiO_2/rGO hydrogel	Bisphenol (BPA)	20 mg	60	UV light 500 W Hg lamp	44
10.	rGO-ZnS-CuS	Ofloxacin	20 mg	86.65	Visible light 300 W Tungsten lamp	Present study

Consequently, it is expected that this strategy will pave the way for efficient catalysts for applications in water purification, air treatment, and energy conversion.

■ ASSOCIATED CONTENT

ⓢ Supporting Information

The Supporting Information is available free of charge at https://pubs.acs.org/doi/10.1021/acsomega.3c03883.

Additional data for BET analysis of rGO-ZnS and rGO-CuS (Figure S1), Photoluminescence spectra (PL) of rGO-ZnS, rGO-CuS and rGO-ZCS NC, (Figure S2), Electrochemical impedance spectroscopy (EIS) of rGO-ZnS, rGO-CuS and rGO-ZCS NC, (Figure S3), Elemental mapping and EDX analysis of rGO-ZCS NC after five cycles (Figure S4), XRD analysis of rGO-ZCS NC before and after five cycles stability test (Figure S5), and ICP/OES analysis of rGO-ZCS NC after five cycles stability test (S6) (PDF)

■ AUTHOR INFORMATION

Corresponding Author

Junghwan Kim − *Department of Materials System Engineering, Pukyong National University, Busan 48513, Republic of Korea;* ⓞ orcid.org/0000-0003-3017-5330; Phone: +82-51-629-6372; Email: junghwan.kim@pknu.ac.kr

Authors

Shanmugam Mahalingam − *Department of Materials System Engineering, Pukyong National University, Busan 48513, Republic of Korea*

Yalini Devi Neelan − *Department of Materials Science and Engineering, Chungnam National University, Daejeon 34134, Republic of Korea*

Senthil Bakthavatchalam − *Department of Chemistry, Faculty of Engineering and Technology, SRM Institute of Science and Technology, Ramapuram Campus, Chennai 600089, India*

Latifah A. Al-Humaid − *Department of Botany and Microbiology, College of Science, King Saud University, Riyadh 11451, Saudi Arabia*

Nora Dahmash Al- Dahmash − *Department of Botany and Microbiology, College of Science, King Saud University, Riyadh 11451, Saudi Arabia*

Harikrishnan Santhanam − *Department of Mechanical Engineering, Kings Engineering College, Chennai 602117, India*

Tae-Youl Yang − *Department of Materials Science and Engineering, Chungnam National University, Daejeon 34134, Republic of Korea;* ⓞ orcid.org/0000-0002-8146-0521

Nazmul Hossain − *Department of Materials System Engineering, Pukyong National University, Busan 48513, Republic of Korea*

Sung Heum Park − *Department of Physics, Pukyong National University, Busan 48513, Republic of Korea;* ⓞ orcid.org/0000-0001-5701-660X

Complete contact information is available at:
https://pubs.acs.org/10.1021/acsomega.3c03883

Notes

The authors declare no competing financial interest.

■ REFERENCES

(1) Wu, Q.; Lu, D.; Kondamareddy, K. K.; Ho, W.; Cao, D.; Zeng, Y.; Zhang, B.; Zhang, Y.; Xie, L.; Zhao, B.; Wang, Z.; Hao, H.; Fan, H.; Wang, H. Highly efficient photocatalytic degradation for antibiotics and mechanism insight for Bi_2S_3/g-C_3N_4 with fast interfacial charges transfer and excellent stability. *Arab. J. Chem.* **2022**, *15*, 103689.

(2) Briffa, J.; Sinagra, E.; Blundell, R. Heavy metal pollution in the environment and their toxicological effects on humans. *Heliyon.* 2020, 6, No. e04691.

(3) Xu, Y.; Liu, J.; Xie, M.; Jing, L.; Yan, J.; Deng, J.; Xu, H.; Li, H.; Xie, J. Graphene oxide-modified LaVO₄ nanocomposites with enhanced photocatalytic degradation efficiency of antibiotics. *Inorg. Chem. Front.* 2018, 5, 2818−2828.

(4) Lellis, B.; Favaro-Polonio, C. Z.; Pamphile, J. A.; Polonio, J. C. Effects of textile dyes on health and the environment and bioremediation potential of living organisms. *Biotechnology Research and Innovation.* 2019, 3, 275−290.

(5) Chen, X.; Memon, H. A.; Wang, Y.; Marriam, I.; Tebyetekerwa, M. Circular Economy and Sustainability of the Clothing and Textile Industry. *Materials Circular Economy.* 2021, 3, 12.

(6) Oluwole, A. O.; Olatunji, O. S. Photocatalytic degradation of tetracycline in aqueous systems under visible light irradiation using needle-like SnO₂ nanoparticles anchored on exfoliated gC₃N₄. *Environ. Sci. Eur.* 2022, 34, 1−14.

(7) Patel, M.; Kumar, R.; Kishor, K.; Mlsna, T.; Pittman, C. U.; Mohan, D. Pharmaceuticals of Emerging Concern in Aquatic Systems: Chemistry, Occurrence, Effects, and Removal Methods. *Chem. Rev.* 2019, 119, 3510−3673.

(8) Papagiannaki, D.; Belay, M. H.; Gonçalves, N. P. F.; Robotti, E.; Bianco-Prevot, A.; Binetti, R.; Calza, P. From monitoring to treatment, how to improve water quality: The pharmaceuticals case. *Chem. Eng. J. Advances.* 2022, 10, 100245.

(9) Cao, H. L.; Cai, F. Y.; Yu, K.; Zhang, Y. Q.; Lü, J.; Cao, R. Photocatalytic degradation of tetracycline antibiotics over CdS/ nitrogen-doped-carbon composites derived from *in situ* carbonization of metal-organic frameworks. *ACS Sustain. Chem. Eng.* 2019, 7, 10847−10854.

(10) Elmolla, E. S.; Chaudhuri, M. Photocatalytic degradation of amoxicillin, ampicillin and cloxacillin antibiotics in aqueous solution using UV/TiO₂ and UV/H₂O₂/TiO₂ photocatalysis. *Desalination.* 2010, 252, 46−52.

(11) Elmolla, E. S.; Chaudhuri, M. Photocatalytic degradation of amoxicillin, ampicillin and cloxacillin antibiotics in aqueous solution using UV/TiO₂ and UV/H₂O₂/TiO₂ photocatalysis. *Desalination.* 2010, 252, 46−52.

(12) Yi, Z.; Wang, J.; Jiang, T.; Tang, Q.; Cheng, Y. Photocatalytic degradation of sulfamethazine in aqueous solution using ZnO with different morphologies. *R Soc. Open Sci.* 2018, 5, 171457.

(13) Okeke, E. S.; Chukwudozie, K. I.; Nyaruaba, R.; Ita, R. E.; Oladipo, A.; Ejeromedoghene, O.; Atakpa, E. O.; Agu, C. V.; Okoye, C. O. Antibiotic resistance in aquaculture and aquatic organisms: a review of current nanotechnology applications for sustainable management. *Environmental Science and Pollution Research.* 2022, 29, 69241−69274.

(14) Uddin, T. M.; Chakraborty, A. J.; Khusro, A.; Zidan, B. R. M.; Mitra, S.; Emran, T. B.; Dhama, K.; Ripon, M. K. H.; Gajdacs, M.; Sahibzada, M. U. K.; Hossain, M. J.; Koirala, N. Antibiotic resistance in microbes: History, mechanisms, therapeutic strategies and future prospects. *Journal of Infection and Public Health.* 2021, 14, 1750−1766.

(15) Bai, X.; Chen, W.; Wang, B.; Sun, T.; Wu, B.; Wang, Y. Photocatalytic degradation of some typical antibiotics: Recent advances and future outlooks. *Int. J. Mol. Sci.* 2022, 23, 8130.

(16) Olusegun, S. J.; Larrea, G.; Osial, M.; Jackowska, K.; Krysinski, P. Photocatalytic degradation of antibiotics by superparamagnetic iron oxide nanoparticles. *Tetracycline case. Catalysts.* 2021, 11, 1243.

(17) Gaim, Y. T.; Yimanuh, S. M.; Kidanu, Z. G. Enhanced photocatalytic degradation of amoxicillin with Mn-doped Cu₂O under sunlight irradiation. *J. Compos. Sci.* 2022, 6, 317.

(18) Zambrano, J.; García-Encina, P. A.; Jiménez, J. J.; López-Serna, R.; Irusta-Mata, R. Photolytic and photocatalytic removal of a mixture of four veterinary antibiotics. *J. Water Process Eng.* 2022, 48, 102841.

(19) Gheytanzadeh, M.; Baghban, A.; Habibzadeh, S.; Jabbour, K.; Esmaeili, A.; Mohaddespour, A.; Abida, O. An insight into tetracycline photocatalytic degradation by MOFs using the artificial intelligence technique. *Sci. Rep.* 2022, 12, 6615.

(20) Rajabi, H. R.; Sajadiasl, F.; Karimi, H.; Alvand, Z. M. Green synthesis of zinc sulfide nanophotocatalysts using aqueous extract of *Ficus Johannis* plant for efficient photodegradation of some pollutants. *J. Mater. Res. Technol.* 2020, 9, 15638−15647.

(21) Das, P.; Tantubay, K.; Ghosh, R.; Dam, S.; Baskey, M. Transformation of CuS/ZnS nanomaterials to an efficient visible light photocatalyst by 'photosensitizer' graphene and the potential antimicrobial activities of the nanocomposites. *Environ. Sci. Pollut. Res. Int.* 2021, 28, 49125−49138.

(22) Isac, L.; Cazan, C.; Andronic, L.; Enesca, A. CuS-Based nanostructures as catalysts for organic pollutants photodegradation. *Catalysts.* 2022, 12, 1135.

(23) Shi, W.; Hao, C.; Fu, Y.; Guo, F.; Tang, Y.; Yan, X. Enhancement of synergistic effect photocatalytic/persulfate activation for degradation of antibiotics by the combination of photo-induced electrons and carbon dots. *Chem. Eng. J..* 2022, 433, 133741.

(24) Mahalingam, S.; Ayyaru, S.; Ahn, Y. H. Facile one-pot microwave assisted synthesis of rGO-CuS-ZnS hybrid nanocomposite cathode catalysts for microbial fuel cell application. *Chemosphere.* 2021, 278, 130426.

(25) Zhai, S.; Abraham, A. M.; Chen, B.; Fan, Z.; Hu, J.; Cai, Z.; Thangadurai, V. Abundant Canadian pine with polysulfide redox mediating ZnS/CuS nanocomposite to attain high-capacity lithium sulfur battery. *Carbon.* 2022, 195, 253−262.

(26) Yang, L.; Guan, X.; Wang, G. S.; Guan, X. H.; Jia, B. Synthesis of ZnS/CuS nanospheres loaded on reduced graphene oxide as high-performance photocatalysts under simulated sunlight irradiation. *New J. Chem.* 2017, 41, 5732−5744.

(27) Muthukumaran, S.; Ashok kumar, M. Structural, FTIR and photoluminescence properties of ZnS: Cu thin films by chemical bath deposition method. *Mater. Lett.* 2013, 93, 223−225.

(28) Wang, L.; Huang, S.; Sun, Y. Low-temperature synthesis of hexagonal transition metal ion doped ZnS nanoparticles by a simple colloidal method. *Appl. Surf. Sci.* 2013, 270, 178−183.

(29) Barrett, E. P.; Joyner, L. G.; Halenda, P. P. The determination of pore volume and area distributions in porous substances. I. Computations from nitrogen isotherms. *J. Am. Chem. Soc.* 1951, 73, 373−380.

(30) Ma, H. Y.; Zhao, L.; Guo, L. H.; Zhang, H.; Chen, F. J.; Yu, W. C. Roles of reactive oxygen species (ROS) in the photocatalytic degradation of pentachlorophenol and its main toxic intermediates by TiO₂/UV. *J. Hazard. Mater.* 2019, 369, 719−726.

(31) Su, Q.; Li, J.; Yuan, H.; Wang, B.; Wang, Y.; Li, Y.; Xing, Y. Visible-light-driven photocatalytic degradation of ofloxacin by g-C₃N₄/NH₂-MIL-88B (Fe) heterostructure: Mechanisms, DFT calculation, degradation pathway and toxicity evolution. *Chem. Eng. J.* 2022, 427, 131594.

(32) Li, Y.; Zhan, J.; Huang, L.; Xu, H.; Li, H.; Zhang, R.; Wu, S. Synthesis and photocatalytic activity of a bentonite/gC₃N₄ composite. *RSC Adv.* 2014, 4, 11831−11839.

(33) Cushing, S. K.; Li, J.; Meng, F.; Senty, T. R.; Suri, S.; Zhi, M.; Li, M.; Bristow, A. D.; Wu, N. Photocatalytic Activity Enhanced by Plasmonic Resonant Energy Transfer from Metal to Semiconductor. *J. Am. Chem. Soc.* 2012, 134, 15033−15041.

(34) Lv, M.; Yang, L.; Wang, X.; Cheng, X.; Song, Y.; Yin, Y.; Liu, H.; Han, Y.; Cao, K.; Ma, W.; Qi, G.; Li, S. Visible-light photocatalytic capability and the mechanism investigation of a novel PANI/Sn₃O₄ p-n heterostructure. *RSC Adv.* 2019, 9, 40694−40707.

(35) D., N.; Kondamareddy, K. K.; Bin, H.; Lu, D.; Kumar, P.; Dwivedi, R. K.; Pelenovich, V. O.; Zhao, X.-Z.; Gao, W.; Fu, D. Enhanced visible light photodegradation activity of RhB/MB from aqueous solution using nanosized novel Fe-Cd co-modified ZnO. *Sci. Rep.* 2018, 8, 10691.

(36) Sodeinde, K. O.; Olusanya, S. O.; Lawal, O. S.; Sriariyanun, M.; Adediran, A. A. Enhanced adsorptional-photocatalytic degradation of chloramphenicol by reduced graphene oxide-zinc oxide nanocomposite. *Sci. Reports.* 2022, 12, 1217054.

(37) Mansingh, S.; Acharya, R.; Martha, S.; Parida, K. M. Pyrochlore $Ce_2Zr_2O_7$ decorated over rGO: A photocatalyst that proves to be efficient towards the reduction of 4-nitrophenol and degradation of ciprofloxacin under visible light. *Phys. Chem. Chem. Phys.* **2018**, *20*, 9872−9885.

(38) Khataee, A.; Sadeghi Rad, T.; Nikzat, S.; Hassani, A.; Aslan, M. H.; Kobya, M.; Demirbaş, E. Fabrication of NiFe layered double hydroxide/reduced graphene oxide (NiFe-LDH/rGO) nanocomposite with enhanced sonophotocatalytic activity for the degradation of moxifloxacin. *Chem. Eng. J.* **2019**, *375*, 122102.

(39) Dong, S.; Sun, J.; Li, Y.; Yu, C.; Li, Y.; Sun, J. $ZnSnO_3$ hollow nanospheres/reduced graphene oxide nanocomposites as high-performance photocatalysts for degradation of metronidazole. *Appl. Catal., B* **2014**, *144*, 386−393.

(40) Yang, J.; Shi, Q.; Zhang, R.; Xie, M.; Jiang, X.; Wang, F.; Cheng, X.; Han, W. $BiVO_4$ quantum tubes loaded on reduced graphene oxide aerogel as efficient photocatalyst for gaseous formaldehyde degradation. *Carbon.* **2018**, *138*, 118−124.

(41) Wang, X.; Wang, A.; Ma, J. Visible-light-driven photocatalytic removal of antibiotics by newly designed $C_3N_4@ MnFe_2O_4$-graphene nanocomposites. *J. Hazard. Mater.* **2017**, *336*, 81−92.

(42) Yu, Y.; Yan, L.; Cheng, J.; Jing, C. Mechanistic insights into TiO_2 thickness in $Fe_3O_4@TiO_2$-GO composites for enrofloxacin photodegradation. *Chem. Eng. J.* **2017**, *325*, 647−654.

(43) Ni, J.; Xue, J.; Xie, L.; Shen, J.; He, G.; Chen, H. Construction of magnetically separable NiAl LDH/Fe_3O_4-rGO nanocomposites with enhanced photocatalytic performance under visible light. *Phys. Chem. Chem. Phys.* **2018**, *20*, 414−421.

(44) Chen, F.; An, W.; Li, Y.; Liang, Y.; Cui, W. Fabricating 3D porous $PANI/TiO_2$-graphene hydrogel for the enhanced UV-light photocatalytic degradation of BPA. *Appl. Surf. Sci.* **2018**, *427*, 123−132.